Journal of Power Sources 190 (2009) 92–102

Contents lists available at ScienceDirect

Journal of Power Sources

journal homepage: www.elsevier.com/locate/jpowsour

Characterisation of mechanical behaviour and coupled electrical properties of polymer electrolyte membrane fuel cell gas diffusion layers

J. Kleemann[a,*], F. Finsterwalder[a], W. Tillmetz[b]

[a] Department of MEA and Stack Technology, Daimler AG, Wilhelm-Runge-Str. 11, D-89081 Ulm, Germany
[b] Zentrum für Sonnenenergie- und Wasserstoff-Forschung, Helmholtzstraße 8, D-89081 Ulm, Germany

ARTICLE INFO

Article history:
Received 12 June 2008
Received in revised form 20 August 2008
Accepted 8 September 2008
Available online 18 September 2008

Keywords:
Polymer electrolyte membrane fuel cell
Gas diffusion layer
Compression
Mechanical simulation
Electrical conductivity
Contact resistance

ABSTRACT

Local compression distribution in the gas diffusion layer (GDL) of a polymer electrolyte membrane fuel cell (PEMFC) and the associated effect on electrical material resistance are examined. For this purpose a macroscopic structural material model is developed based on the assumption of orthotropic mechanical material behaviour for the fibrous paper and non-woven GDLs. The required structural material parameters are measured using depicted measurement methods. The influence of GDL compression on electrical properties and contact effects is also determined using specially developed testing tools. All material properties are used for a coupled 2D finite element simulation approach, capturing structural as well as electrical simulation in combination. The ohmic voltage losses are evaluated assuming constant current density at the catalyst layer and results are compared to cell polarisation measurements for different materials.

The results show that the largest part of the polarisation difference found between roll-good and batch type materials with wide channel flowfields is well captured by the simulation and is due to additional electrical losses in the locally low compressed GDL. Thus, for the first time a broader understanding of the significant performance impact of diffusion layer mechanical properties is generated. However, at higher loads an interaction of compression with electrical and additional heat and mass transport effects occurs, which will be included in the next part of the study. This part is limited to structural mechanics and coupled electrical transport effects.

1. Introduction

PEM fuel cells are probably the most promising candidates in terms of future emission free propulsion. However, a couple of drawbacks today still impede the broad rollout of this technology. One of the major issues to be resolved are the relatively high costs of a PEM fuel cell system compared to those of an internal combustion engine. Competitive price cannot be merely achieved by the economies of scale, but progress in terms materials and power density is also needed [1,2]. Cheaper materials have to be identified and, where this comes to a limit, power density in terms of W m^{-2} active cell area has to be increased to minimize the use of the pricy components at a given total power ratio.

Besides precious metal and membrane, one of the cost driving components inside a PEM fuel cell are the gas diffusion layers (GDLs), typically consisting of a carbon fibre paper, non-woven or cloth [2]. Common standard today are batch produced papers that undergo a costly production process of resin binding and graphitisation at high temperatures, determining their relatively high price. Favourable low-cost materials are continuous roll-goods with no, lower or non-graphitized binder and lower energy demand in production. Another benefit for roll-good GDLs is the potential simplification of the membrane-electrode-assembly (MEA) manufacturing process, where additional cost reduction can be achieved when shifting from batch to roll processes [3].

However, these roll-good materials typically show disadvantages in cell performance when used in conventional cell designs compared to the highly graphitic bound standard sheet types, as, e.g. TGP-H-060 (Fig. 1).

Reasons for this discrepancy were unclear and therefore investigated in the depicted studies. Typically considered material parameters of both material classes like gas permeability or electrical conductivity under high compression do not show any obvious differences that could explain the severe performance loss [46]. However, a higher gas pressure drop along the cell's gas flow field channels could be measured using roll-good materials. This could not be explained by intrinsic material permeability difference, but was attributed to a higher GDL blocking rate of the channels under

* Corresponding author. Tel.: +49 731 505 2996; fax: +49 711 3052 180140.
E-mail address: joerg.kleemann@daimler.com (J. Kleemann).

0378-7753/$ – see front matter © 2008 Elsevier B.V. All rights reserved.
doi:10.1016/j.jpowsour.2008.09.026

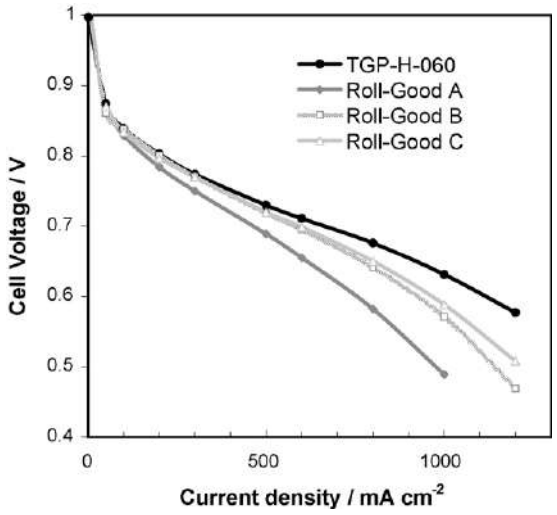

Fig. 1. Polarisation curves measured with different GDL materials (sheet and roll-good) under automotive conditions in a wider channel flowfield (>2 mm).

compression when using these materials. Performance does not drop dramatically with slightly increasing gas pressure drop, but the higher pressure drop in turn hints to a lower compression of these types of material under the flow field channels, leading to a partial blocking of the channel by the bulging GDL. On the other hand most of the critical material parameters in terms of performance like electrical and thermal conductivity, as well as gas permeability and diffusivity are highly depending on the compression rate of the fibre materials [3–5].

Visual investigations using an optical microscope and a compressed cross-section channel setup including the GDL revealed that there is drastically less compression of the material in channel sections when using different roll-good materials compared to highly bonded batch-fabrication types, thus confirming the assumptions based on the measured pressure drop differences.

Fig. 2 shows a comparison between compression behaviour of batch produced TGP-H-060 (a) and a commercial non-woven (b). The compressed thickness of the stiff TGP slowly increases from the landing edge to the channel centre and does not reach uncompressed material thickness in the centre, indicating that the material transports a certain amount of compression pressure to the channel centre even at channels wider than 2 mm. The roll-good non-woven on the other hand returns to its initial thickness proximate to the landing edge, indicating a poor compression transport

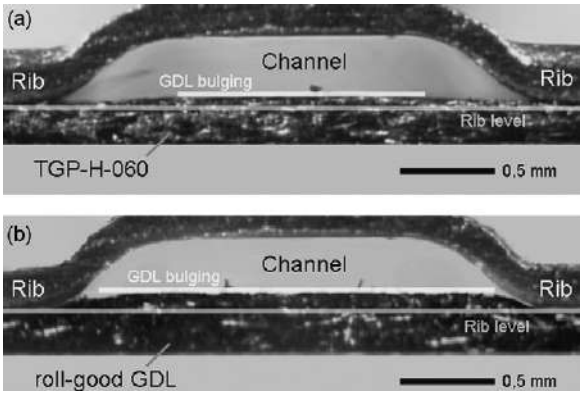

Fig. 2. GDL compression distribution mapped in a compressed microscopic flowfield cross-section setup for TGP-H060 (a) and a commercial roll-good GDL (b). The roll-good GDL is hardly compressed under the channel.

into the channel by this material type and thus vanishing compression pressure to the catalyst layer at wider channels. However, a distinct gap between GDL and active layer could be found with none of the tested materials.

To confirm the differences in intrinsic material compression in channel sections, a film measurement technique was used to asses pressure distribution under the GDL for different materials. A highly sensitive pressure tracing film was applied between GDL and catalyst layer and local pressure distribution was estimated after the test based on local colour intensity using a scanner and a calibration curve. Although results were very limited in terms of quantifiable results [6], channel centre compression pressure was significantly lower for all tested roll-good materials compared to TGP-H-060.

From these findings it becomes obvious that a reliable quantitative method is needed to predict local GDL compression over the channel–landing interface and to estimate performance losses associated with a reduced local compression under channel sections.

Though a couple of studies can be found in literature on optimized external fuel cell stack compression [7–12], studies on compression distribution inside the GDL and its effects on performance are scarce. Most of the publications focus on optimizing of the GDL–bipolar plate contact [9] or on mass transport effects [7,11,12]. A couple of modelling studies were presented that account for anisotropic conductivity of the gas diffusion layer, but do not consider material compression as a parameter [13–16]. Recently, Nitta et al. carried out investigations on inhomogeneous compression distribution in the GDL and its effects on temperature distribution and electrical conduction [17–20]. However, they did not incorporate the real GDL compression distribution for different GDL materials or different channel–landing geometries into their model, but assumed that the regarded GDL type is virtually uncompressed in channel sections following an arbitrary compression shape function. They come to the conclusion that inhomogeneous GDL compression does not affect overall cell performance significantly under the given assumptions, but has high impact on the current density distribution. Some mechanical modelling of the GDL–flowfield structure under compression was presented by Zhou et al. [7,9,11], however, assuming isotropic [9] or quasi-isotropic [7,11] mechanical behaviour in the GDL and focusing on the bipolar plate contact and the porosity change. Models used in [7,11] could be described as quasi-isotropic because material constants required for orthotropic or even fully anisotropic behaviour like shear modulus and Poisson ratio are not specified. A similar case can be found in the report of Freunberger et al. [21], where an orthotropic structural model for the GDL is presented, but the shear modulus is calculated using a solely isotropic relation. In their study, modelled compression was used to interpret micro-wire potential measurements in terms of sub-mm current distribution.

In the following study a simulative approach was chosen together with an intense material characterisation effort to help predict and optimize GDL compression and associated performance effects reliably. This will be subject to the following sections, starting with a simulative approach to predict GDL compression and pressure distribution under the flowfield by means of Finite Element Method and later on coupling electrical transport properties of the GDL to the actual local compression calculated.

2. GDL mechanical modelling approach

Due to the complex structure of the GDL–flowfield interface and the anisotropic nature of a GDL, a simple analytical solution of the deformation problem is not feasible. Discretized simulation techniques like the Finite Element Method (FEM) together with detailed

material characterisation have to be applied to access the problem and to set the relation between external stresses applied and strains occurring inside the material. Deformation or strain in an object is generally described in 3-dimensional euklidic space using the symmetric Cauchy–Green strain tensor ε_{ij} ($i,j = x,y,z$) that specifies the displacement of neighbouring elements in relation to each other [22,23]. The deformations inside the body are caused by stresses that result, for example from external forces. These stresses are specified as ratio of force per unit area and can be given for a certain point inside the body using a rank-two tensor, corresponding to the formulation of strains [23–25]. As for strains, the components of the stress tensor can also be subdivided into components with even notation referring to normal stresses σ_{ii} and components with mixed notation referring to shear stresses τ_{ij}, satisfying $\tau_{ij} = \tau_{ji}$. A fundamental relation between stresses and strains inside a linear elastic material is introduced by generalized Hooke's law that offers a good starting point for the GDL model formulation, even if the assumption of linear elasticity has to be verified or corrected. The governing equation for Hooke's law introduces a rank-four tensor called elasticity tensor C that attaches strains in any given direction to stresses in any further direction, wherein the directions of stresses and strains do not necessarily coincide [23,25–29]. In index notation, Hooke's law can be written as

$$\sigma_{ij} = C_{ijkl}\varepsilon_{kl} \tag{1}$$

For a fully anisotropic material it can be shown that 21 independent elasticity constants C_{ijkl} exist [23,28,29], which, however, can be reduced significantly in the given case.

Measurement effort would be hardly feasible at this number, especially if the inhomogeneous GDL microstructure of fibres, binders, fillers and pores would be accounted for by using locally deviating elasticity constants. If stresses and strains in single fibres are not of interest and the dimensions considered are large compared to fibre and pore dimensions, a macro-structural approach applying a homogenized microstructure can be chosen [26]. In this case, fibres and other material constituents are "smudged" and replaced by statistic average characteristics of the bulk material.

In spite of this homogenized view, the directionality of the bulk material properties cannot be neglected. It can be assumed that mechanical properties of the bulk material are mainly dominated by the fibre structure and by the way those fibres are connected [27,30]. For most of the regarded materials, the vast amount of fibres is oriented in the material plane, so that different mechanical properties can be expected along and across the plane (Fig. 3) [3]. Many of the given materials also show a direction of preferred fibre orientation in the plane, typically referred to as the machine direction (MD). Thus, three directions can be distinguished in common gas diffusion layer materials that are oriented perpendicular to each other: the through-plane direction across the material thickness (TPD), as well as the machine direction (MD) and the cross-machine direction (CMD) in the material plane. Along these directions the material properties can be assumed constant, so that symmetry planes can be spanned perpendicular to those directions. This allows to switch from a fully anisotropic to an orthotropic material model. The assumption of orthotropic behaviour is also very common for most types of fibre composite materials, as well as for technical woods or textured, cold-rolled sheet metal [29]. It is consequent to use this model based on the mentioned considerations also for fibrous gas diffusion layer materials, thus reducing the independent material coefficients of C to 9.

Furthermore, typical flowfield geometries consist of straight, uniform channels over a vast part of the cell, so that symmetry planes can be assumed at an arbitrary position perpendicular to the channel direction z. Thus, stresses at the presumed plane section have to be in balance and all strains in z-direction turn zero [25,29].

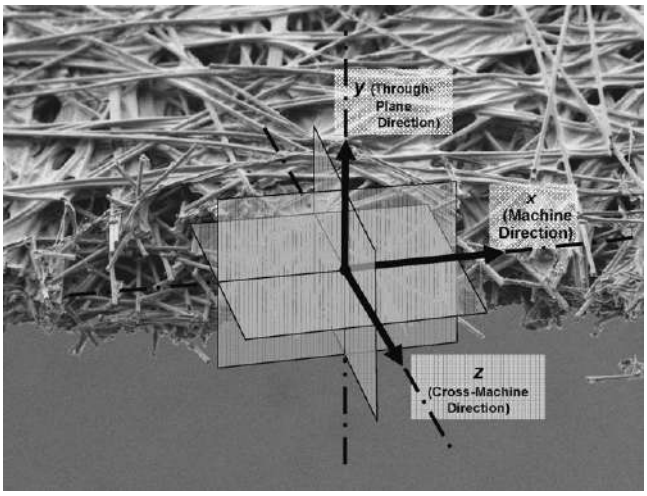

Fig. 3. SEM cross-section and fibre structure of TGP-H-060 with virtual (macroscopic) symmetry planes. Fibres are mainly oriented in the material plane, symmetry planes can be put up perpendicular to through-plane (TPD), machine (MD) and cross-machine direction (CMD).

A plane strain condition is achieved, leaving only 4 independent material coefficients of C to be determined.

To make elasticity matrix coefficients determinable in terms of simple measurement methods, they have to be expressed in terms of engineer's constants defined in simple uniaxial stress conditions [26] like Young's (E_x, E_y) and shear moduli (G_{xy}) or Poisson's ratio (ν_{xy}). This leads to a formulation of Hooke's law for the GDL materials as is given in Eq. (2) for the orthotropic plane strain case [29]:

$$\begin{bmatrix} \sigma_x \\ \sigma_y \\ \tau_{xy} \end{bmatrix} = \begin{bmatrix} \dfrac{E_x}{1-\nu_{xy}\nu_{yx}} & \dfrac{\nu_{xy}E_y}{1-\nu_{xy}\nu_{yx}} & 0 \\ & \dfrac{E_y}{1-\nu_{xy}\nu_{yx}} & 0 \\ \text{Symm} & & G_{xy} \end{bmatrix} \begin{bmatrix} \varepsilon_x \\ \varepsilon_y \\ 2\varepsilon_{xy} \end{bmatrix} \tag{2}$$

Unlike in the isotropic case where Young's modulus, shear modulus and Poisson's ratio are coupled, these parameters are totally independent in the orthotropic case and have to be measured separately.

3. Measuring mechanical GDL properties

Measurement methods have been developed to determine all four independent material constants E_x, E_y, G_{xy}, and ν_{xy} in macroscopic approach. For all the testing methods depicted below, a minimum of three samples from the same lot was tested and average results are given also indicating the standard deviation.

3.1. Measurement of Young's modulus in the material plane E_x

Young's modulus in the material plane of a sheet material can be determined using different loading conditions like tension, compression or bending. These differing cases can deliver slightly differing results for E_x, especially if porous fibre materials are tested. Therefore a material test for determination of E_x is preferred that is as close as possible to stress conditions in x-direction inside the material in a fuel cell, which typically consist of a mixture of tension and compression. Deformation behaviour of the GDL in the flowfield as shown in Fig. 2 indicates that the material centre line performs a complex Ω-shaped deformation curve with contrary zones of tension and compression on either side.

This is a typical bending case, that is well captured in 2-point, 3-point or 4-point bending tests. These testing methods are widely

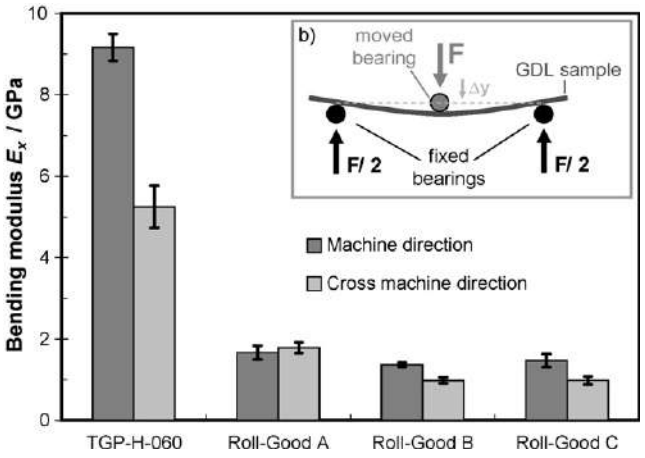

Fig. 4. Measured bending moduli E_x for different GDLs in machine and cross-machine direction (a) and 3-point bending setup for determination of GDL bending modulus E_x (b).

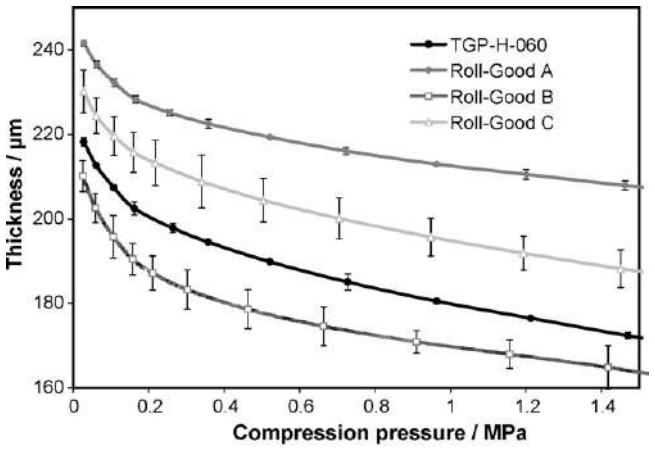

Fig. 5. Measured GDL thickness over compression pressure for different samples.

described in literature and standardisation for various types of materials, among those also papers and non-wovens [31–34]. For the sake of reproducibility and easy implementation a 3-point bending test was chosen following [31,32].

A device consisting of two cylindrical bearings of 6 mm diameter in variable distance between 20 and 60 mm was constructed (Fig. 4b), that could be fixed to a material tester (Zwick–Roell, type Zwicki) equipped with a precision 20 N force sensor. Quadratic material samples of 70 mm side length were cut using a jig and could be applied in both directions to test machine as well as cross-machine direction. Prior to testing, the samples thickness was measured using a stylus. During bending, force was applied using an additional cylindrical bearing with identical diameter fixed to the force sensor and the moving part of the material tester that was centred parallel to the fixed bearings. Displacement was measured using the machines internal traverse sensor. Young's modulus in x-direction was calculated using Eq. (3) following [33], where the slope for $\Delta F/\Delta y$ was taken as an average between 35% and 100% of maximum displacement.

$$E_x = \frac{\Delta F}{\Delta y}\frac{l^3}{4bh^3} \tag{3}$$

A minimum of three samples of each type of material was measured in machine and in cross-machine direction. All tested samples were found to show a highly linear bending behaviour in the tested strain range. However, the results in E_x showed drastic differences between the different GDL types (Fig. 4a). While the TGP samples showed bending moduli in the range of up to 10 GPa and were in good agreement with the manufacturers data sheet [46], all tested roll-good GDLs were found to lie up to an order of magnitude lower. Most of the samples showed a distinct directionality of the measured bending modulus, depending if tested in machine or cross-machine direction.

3.2. Measurement of Young's modulus through the material plane E_y

The loading condition inside a GDL in y-direction perpendicular to the material plane is more obvious than in the material plane. Compressive stress is exerted by the flowfield landings and, as seen in Fig. 2, depending on the GDL-properties more or less spread over the landing and channel span. Measurement of Young's modulus in y-direction E_y should therefore consequently be carried out under compressive load.

A fixture was designed to test circular GDL samples of 40 mm diameter for thickness under compressive stress using the material tester mentioned above equipped with a 2500 N force sensor. Because of the limited thickness of the samples and the higher forces applied during the test, actual sample thickness was measured using three high-resolution inductive distance sensors (Baumer electric) that were fixed to the device as close as possible around the sample and the actual thickness could be averaged. Samples were tested for thickness at compression pressure of up to approx. 1.8 MPa at continuously increasing compressive load over 120 s.

All tested materials showed a non-linear, declining compression behaviour with more or less pronounced material hardening at high strains (Fig. 5). This is comprehensible considering the decreasing amount of pores and the increase in fibre contact points during compression and has been described in literature [3,4]. In terms of material modelling, this means that a constant E_y is not sufficient to reflect the materials compression behaviour as first intended using Hooke's law. Young's modulus in y-direction has to be expressed as a function of compression itself $E_y = f(\varepsilon_y)$. The particular value for E_y at a certain compression $\varepsilon_{y,1}$ has been calculated using a secant modulus $E_{y,1}$

$$E_{y,1} = \frac{\sigma_{y,1}}{\varepsilon_{y,1}} \tag{4}$$

where σ_y is the compressive force applied per square area of the sample and ε_y is the ratio of thickness change to initial thickness (Eq. (4)). The dependency $E_y = f(\varepsilon_y)$ was expressed using a polynomial fit function, that was fitted to the experimentally measured data for each material and used as an input for the structural simulation.

3.3. Measurement of Poisson's ratio ν_{xy}

Poisson's ratio is crucial to predict transverse strain under load in a certain direction. For isotropic materials, Poisson's ratio can be calculated from Young's and shear modulus, however, for orthotropic materials it is totally decoupled. Inside the GDL, the highest strain typically occurs in y-direction as a compression of the material under the flowfield landings. A high Poisson rate of the GDL material would mean that a spreading of the material in x-direction could be expected coupled with the material compression in y-direction under the flowfield landings, possibly even leading to a GDL lift-off from the active layer in the channel centre.

A setup was developed to quantify the transverse strain coupling, using a stack of 5 GDL-samples of 5 mm in diameter that

were compressed perpendicular to the material plane in y-direction using a spring clamping fixture. Thickness of the stack was measured before and after compression using an optical microscope, and also the change in sample diameter in the middle of the stack was determined in the same way. A PTFE-film was attached to both clamping surfaces to reduce friction of the GDL-material to the fixture and to allow for transverse movement. Poisson ratio ν_{xy} was calculated based on Eq. (5), calculating compression strain ε_y and transverse strain ε_x from the optical measurements:

$$\nu_{xy} = -\frac{\varepsilon_y}{\varepsilon_x} \tag{5}$$

Measured values of ν_{xy} were found to be approximately zero within the standard deviation for all tested materials in machine as well as in cross-machine direction. This could have been anticipated regarding the porous microstructure of the materials, where the volume reduction during compression can be explained by reduction of pore volume. Based on this finding that $\nu_{xy} \approx 0$, the elasticity matrix from Eq. (2) can be further simplified and the transverse coupling coefficients can be removed:

$$\begin{bmatrix} \sigma_x \\ \sigma_y \\ \tau_{xy} \end{bmatrix} = \begin{bmatrix} E_x & 0 & 0 \\ 0 & E_y & 0 \\ 0 & 0 & G_{xy} \end{bmatrix} \begin{bmatrix} \varepsilon_x \\ \varepsilon_y \\ 2\varepsilon_{xy} \end{bmatrix} \tag{6}$$

3.4. Measurement of shear modulus G_{xy}

The shear modulus gives an indication how easily sections of the material can be staggered against each other, which becomes especially crucial if deformations occur over a short length compared to material thickness. For orthotropic materials and especially for fibre compound structures, shear modulus can be very low compared to Young's modulus in x-direction, so that the shear influence is much higher than in the isotropic case [29]. This gives rise to the assumption that shear modulus is a critical parameter for compression transport from landings to the channel centres in the GDL, given the small channel spans and the typically limited shear stiffness of fibre compound structures.

Through-plane shear modulus G_{xy}, however, was found to be the hardest structural material property to measure for the GDL samples. The low thickness of the materials together with the compressibility made common techniques like varied bearing distance bending following [34] or a single lap method as proposed by Schneider et al. [40] fail. Most other tests found in literature are focused on the in-plane shear modulus of sheet materials, which would refer to G_{xz} using the introduced nomenclature [35–39] and are not useful here.

A different technique to determine G_{xy} was developed following the short-beam bending method in a multipoint load arrangement as depicted for measuring shear strength in [40–42]. Two corresponding, guided matrices were constructed that allow material deformation in the xy-plane at a very short beam length in multiple segments (Fig. 6a). This method, however, could not allow for direct measurement of G_{xy}, since GDL compression above the bearings and bending have significant impact on the deformation. A simulative optimisation study was conducted to optimize gap and bearing width of the matrices for maximum shear influence. A wider gap would pronounce bending influence on the deformation, a very small gap would on the other hand limit deformation to compression of the GDL. Even at optimized gap width, the shear part of the deformation result was found to be limited to 40–70%, depending on the combination of parameters. Because bending and compression behaviour of the materials were determined before, mechanical FEM-simulation of the GDL deformation could be used to correct the measured deflection for bending and compression impact (Fig. 6b). Assumed shear modulus G_{xy} was varied in the simulation applying previously measured bending and compression moduli E_x and E_y for the tested material, until the experimental deformation result was hit giving the final shear modulus G_{xy} for the tested material.

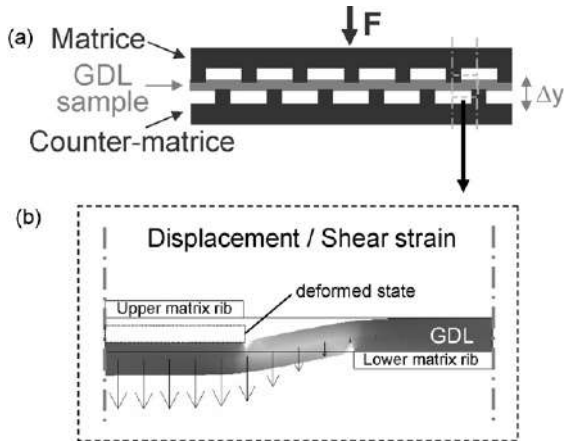

Fig. 6. (a) Multipoint short-beam bending setup for determination of through-plane shear modulus G_{xy}. Bending span was optimized for a maximum shear influence on the result, but still material compression and bending have an impact of around 50% on the measured deflection. (b) Structural FEM-simulation of one bending segment was used to find correction factors for determination of real GDL through-plane shear modulus G_{xy} with known compression E_y and bending properties E_x.

The test was conducted by fixing the matrices to the compression test setup described in Section 3.2, using rectangular GDL samples of 47 mm × 40 mm size. Load was applied at constant rate until breakage.

The results were interpreted using the described simulation approach for deflection measured at 0.5 MPa theoretical shear stress. Deflection curves were roughly linear with compression until breakage for all the tested materials. Thus, the through-plane shear modulus was assumed constant for the further studies. Values for G_{xy} were found to vary between 5 and 12 MPa for the tested roll-good samples and were determined to approx. 20 MPa for the TGP-H-060 samples (Fig. 7). Values in machine and cross-machine direction were found to vary slightly.

Mechanical properties for the different GDL materials are now determined and can be used as an input for the structural simulation of GDL compression under the flowfield landing and channel structure. On the other hand, the impact of compression on transport properties has to be analysed. In this study, the focus will be put on electrical properties inside the GDL and on the electrical contact effects to the adjacent catalyst layer.

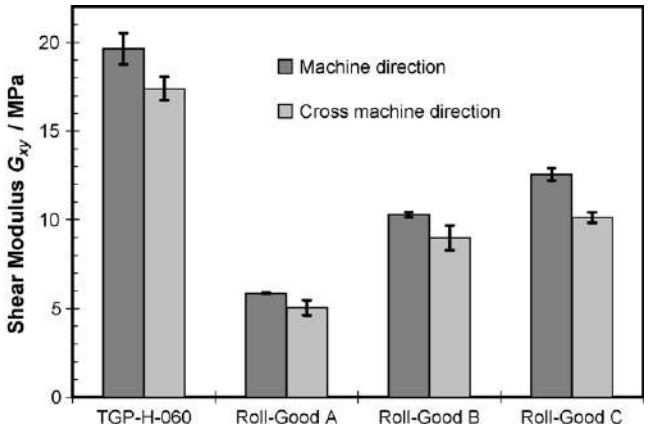

Fig. 7. FEM-corrected shear modulus results G_{xy} for the different GDL types.

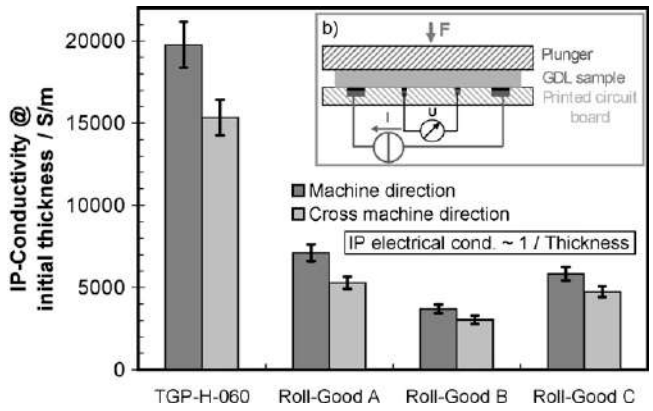

Fig. 8. (a) Measured in-plane conductivities for the different GDLs referring to initial (uncompressed) material thickness. The total resistance measured was found to be compression independent, thus specific material conductivity increases linearly with decreasing thickness. (b) 4-Point setup for GDL in-plane resistance measurement. The setup is based on a printed circuit board with gold coated electrode tracks.

4. Measuring electrical GDL properties as a function of compression

The different slope of polarisation curves measured with batch-produced and roll-good GDL materials hints to differences in ohmic resistance between the cells. This could be accounted to different effects.

Although the GDL through-plane resistance at high compression does not differ significantly between the material classes following the manufacturers' data sheets [e.g. 46], it can be expected that compression has a significant impact on GDL trough-plane bulk conductivity as well as on contact resistances to the adjacent layers [3,4]. Literature studies on these effects, however, are rare to date. Very recently, Nitta et al. have presented measurements on the GDL through-plane resistance and on contact resistances to catalyst layer and flowfield plate [17,19]. They come to the conclusion that GDL bulk through-plane conductivity as well as contact resistance to the catalyst is highly compression dependent.

To evaluate the effect of GDL bulk and contact resistance on cell performance by coupling simulated compression with electrical effects, a detailed study of conductivity dependency on compression has been conducted for the different materials.

4.1. Measurement of GDL in-plane conductivity over compression

Electrical in-plane conductivity of a film material can be measured in a simple 4-point arrangement to exclude contact effects of the current electrodes from the result. A 4-point measuring device was developed based on a printed circuit board consisting of four straight electrodes that were arranged parallely (Fig. 8b). The outer two were used to impress the defined measuring current, the inner two served as potential probes to measure voltage drop over the GDL. The setup was fixed to the material tester between two pressure plates to control GDL compression pressure. At least 3 GDL samples of each type were measured in machine as well as in cross-machine direction, each one cut to a size of 20 mm × 40 mm using a die cutter. Initial thickness of the samples was measured prior to the test using a stylus.

The total resistance between the measuring electrodes was found to be independent of compression pressure for all tested material samples, leading to the conclusion that in-plane conductivity of the GDL increases linearly with decreasing thickness. However, in-plane conductivities at initial thickness were found to deviate up to an order of magnitude between the batch type and roll-good GDLs (Fig. 8a). For the TGP-H-060 samples, conductivities of around 20,000 S m^{-1} were measured at initial thickness, whereas the roll-good samples were in a range between 1500 and 8000 S m^{-1}. Furthermore, the measuring direction had a significant impact on the result for most of the materials.

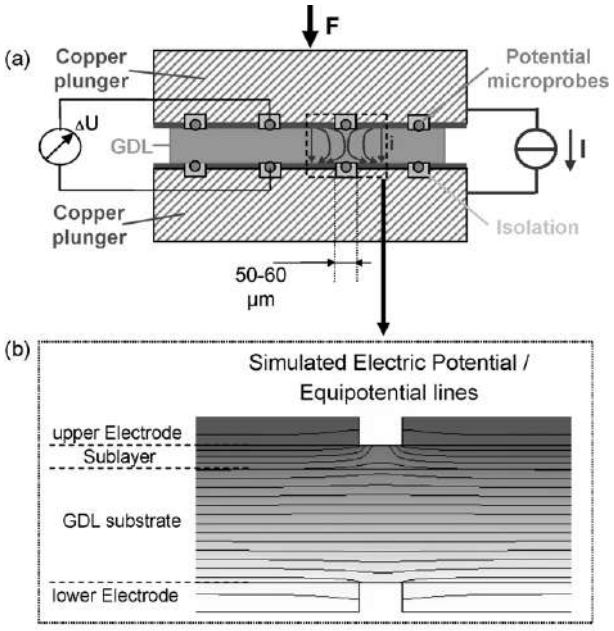

Fig. 9. (a) Microprobe setup for (quasi 4-point) measurement of GDL substrate through-plane resistance over compression and spreading of the measuring current (qualitative). (b) Electrical FEM-validation of the through-plane resistance setup with potential distribution and equipotential lines in the sample: the sublayer is hardly covered with this method.

4.2. Measurement of GDL through-plane conductivity over compression

For the through-plane measurement, resistance of the bulk material had to be separated from the contact resistance to the measuring electrodes, which becomes difficult if thin highly conducting film materials are tested. Although the electrode surfaces were gilded, contact effects could not be neglected. The typical device to exclude contact resistances is a 4-point setup, as it was used for the in-plane measurement. However, it is hard to apply a functional voltage pickup between the current electrodes if a film material of less than 0.5 mm thickness is tested in through-plane direction. Freunberger et al. have placed micro gold wires into an operating cell between catalyst and GDL to measure sub-mm current distribution by determining GDL voltage drop [21]. Following this proposal, a direct application of potential sensing 30 µm micro-wires to the GDL surfaces to exclude contact resistances turned out to be unreliable due to several reasons. However, in an improved setup, the micro-wires were fixed and embedded to the copper measuring electrode surfaces keeping them electrically insulated, and only on the wire surface facing the GDL the insulating coating was removed (Fig. 9a). Similar approaches using embedded microelectrodes have been proposed by Heinzel et al. [43] for measuring through-plane conductivity of graphitic bipolar plates and by Cooper [44] for measuring membrane through-plane conductivity. This approach was found to be more reliable, although large microelectrode sensing gaps would influence the measuring current distribution in their surrounding and therefore falsify the result as already described by Cooper [44]. The minimum microelectrode and insulation span

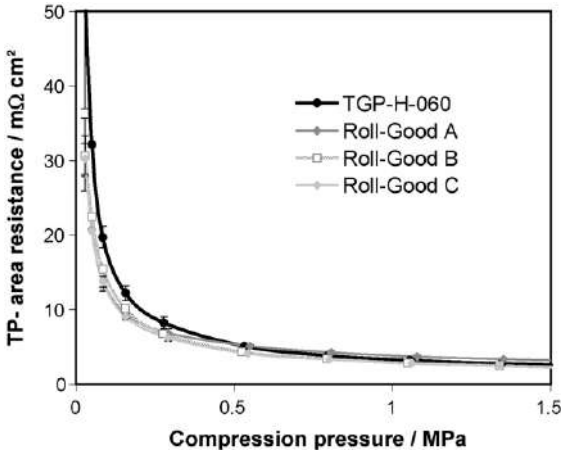

Fig. 10. Measured through-plane area resistance over varied compression for the different GDL samples.

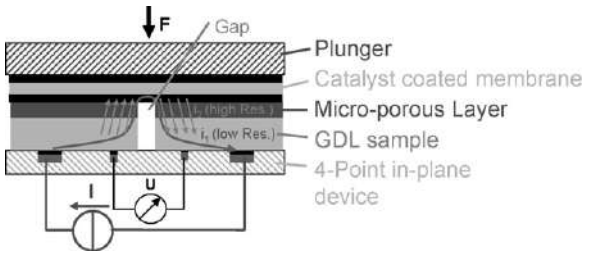

Fig. 11. Measurement setup for determination of sublayer resistance in combination with sublayer-catalyst layer contact resistance over compression. A small gap in the GDL sample is used to force current through the GDL–catalyst layer interface.

that could be achieved with the described preparation technique was in the range of 50–60 μm. An electrical FEM-simulation of the setup was carried out, assuming constant voltage at the copper electrode surface and an insulated microelectrode gap of 60 μm width (Fig. 9b). Simulation results showed for assumed typical GDL substrate through-plane and higher in-plane conductivities, the measurement error with this setup due to current density distortion would be lower than 10%. However, if a GDL with micro-porous layer is regarded and isotropic conductivity is assumed for the micro-porous layer, the measurement will not be able to capture the additional resistance of this layer.

A through-plane measuring device was manufactured based on two gilded copper plates, where 4 micro-wires were embedded isolated to the surface of each electrode, but blanked on the top side. The copper electrodes were fixed to the material tester and the GDL samples were put on. Compression pressure was applied at constant rate, following the compression test described above. A constant measuring current was applied at the copper plates. Measured potential of the 4 voltage probes on either side of the GDL was averaged and the through-plane sheet resistance was calculated using average side-to-side potential drop, measuring current and GDL area.

The results showed that GDL substrate bulk resistivity through the material plane is highly compression dependent and increases progressively at low pressures (Fig. 10). This behaviour was observed for all tested GDL materials, drastic variations between material classes as for the in-plane conductivity could not be found.

The effect of significantly increasing GDL through-plane resistivity at low compression can be expected to influence cell performance if the GDL is hardly compressed under the channel, and therefore should be taken into account in the simulation. GDL through-plane bulk conductivity was expressed as a function over compression pressure inside the material using a polynom regression function in the simulation.

4.3. Measurement of micro-porous layer resistance and catalyst layer contact resistance

All tested GDL types are coated with a micro-porous layer in their finished state, typically consisting of a porous carbon powder structure with a significant amount of PTFE (5–30%). This additional layer sometimes also called sublayer of approx. 30–40 μm thickness improves the GDLs liquid water management capability, protects the membrane from punching fibres and can also be beneficial in terms of electrical and thermal contact to the catalyst layer [3]. However, a remaining electrical contact resistance due to reduced local compression pressure at this interface or a limited conductivity of the electrically isotropic sublayer itself would be of significant impact, because it cannot be compensated by higher in-plane conductivity as for the GDL substrate through-plane conductivity. Mamunya et al. [45] describe a very strong compression dependency of metal powder conductivity, if oxide films or an isolating filler material are involved. This is basically comparable to the sublayer structure, where the high PTFE content acts as isolating filler.

Due the small thicknesses of those layers both effects are hard to measure and therefore rarely treated in literature. A few peel-off tests using an adhesive film to separate micro-porous layer and GDL substrate confirmed a compression dependency of sublayer conductivity in the 4-point in-plane device, but results did not allow quantification.

The contact resistance between GDL and catalyst on the other hand is also difficult to determine and studies in literature are limited to data obtained in combination with membrane resistance [19].

In this study, a setup was developed to determine catalyst layer contact and micro-porous layer resistance in conjunction, since the effect on cell performance can be expected to be similar. A mixed in-plane/through-plane setup was developed, using a catalyst coated membrane (CCM) fixed to two rectangular pieces of sublayer-coated GDL that are separated by a very small gap. The measuring current is applied to the GDL pieces using the above described 4-point device, each piece of GDL contacting one side of the device. The current is thus forced to cross the sublayer and the GDL–catalyst interface at one GDL-piece before it runs laterally in the catalyst layer along the gap and re-enters the other piece of GDL (Fig. 11). The GDL substrate in-plane resistance is known, and the mere catalyst layer resistance has also been determined before using the 4-point device and was found to be independent on compression, but low compared to the GDL in-plane resistance. The lower the sublayer and contact resistance are, the more current will concentrate on the very edge of the gap and the lower the measured voltage drop becomes. The higher the sublayer and contact resistance, the more the measuring current spreads over the interface area and has a longer pathway inside the higher resistive catalyst layer, thus the measured voltage drop increases. The setup was modelled in an electrical FEM-simulation and different cases for the sublayer and contact resistance were simulated, assuming the previously measured GDL substrate and catalyst layer resistance. With this approach, the measured voltage drop could be used to back-calculate the combined sublayer and contact resistance based on the simulation results. The GDL substrate in-plane and through-plane conductivity were found to be of negligible influence on the result. However, GDL gap width was found to be a significant factor on the absolute voltage drop offset and could not be determined precisely in the experiments. Therefore, the sublayer and contact

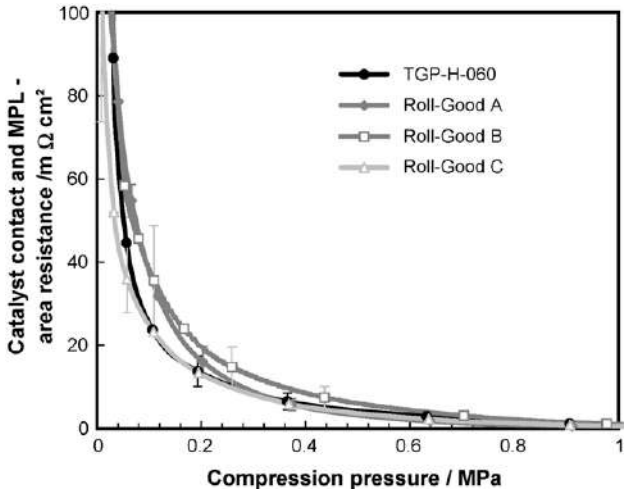

Fig. 12. Measured catalyst layer contact and sublayer area resistance over compression for different GDL samples and the same CCM type. Measured values are in relation to an arbitrary origin at 2 MPa.

resistance were assumed negligible at highest measuring pressure of 2 MPa and the measured voltage drop at this point was used as an offset, so that the increasing voltage drop at lower compression pressure could be used to predict the increase in contact and sublayer resistance. Sublayer and contact resistance could not be separated, but they were found to have the same impact on the result.

The measurement was conducted using the 4-point measuring device described above applied between the pressure plates of the material tester. Two pieces of GDL (20 mm × 20 mm) were fixed to a CCM sample (40 mm × 20 mm) using small glue spots. A constant gap width of approx. 300 μm between the GDLs was controlled using a spacer. On top of the test sample a foam rubber piece was placed to assure homogeneous compression pressure also at the gap edges. The sample was loaded at constant load rate to a compression pressure of 2 MPa and afterwards unloaded under the same condition. During this cycle, a constant measuring current of 2 mA dc was supplied and voltage drop was monitored at the probing electrodes. Contact and sublayer area resistivity increase referring to maximum pressure were evaluated using the measured, off-set corrected voltage drop in the unloading cycle and the correlation function obtained from the simulation.

The results showed a drastic, progressive increase in contact and sublayer area resistivity at low pressures for all tested GDL materials. Quantitative differences could be found between different materials, but the characteristic trend was similar for all tested samples. At least three samples of each material were tested and an average resistivity function for each one is shown in Fig. 12. The measured dependency of resistivity over compression was completely attributed to the GDL sublayer in the ohmic loss simulation and expressed as a polynom regression function.

5. Modelling results and discussion

5.1. Model boundaries and assumptions

The relevant material parameters for mechanical and electrical modelling of the GDL are now determined and can be used as an input for the coupled modelling approach. For this procedure, the structural deformation of the GDL under flowfield compression was modelled based on the orthotropic model presented in Section 2. Linear elastic material properties were assumed based

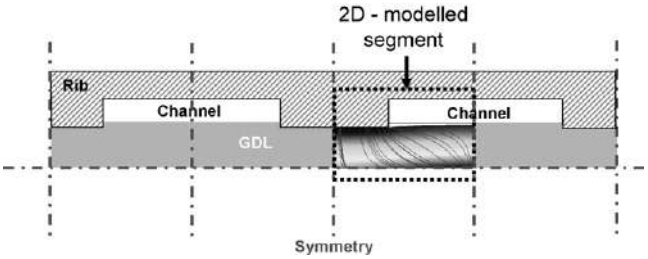

Fig. 13. Domain mapped in the FEM-model with surrounding GDL and flowfield parts. Membrane and catalyst layer are disregarded.

on the measurement findings, except for compression modulus E_y which was expressed as a fitted function of compressive strain ε_y. A symmetric flowfield and GDL setup on cathode and anode was assumed, so that a symmetry boundary could be applied in the membrane plane, setting the y-displacement to 0 there. Symmetry was also assumed at the channel and landing centre, subsequently compensating the x-displacement there to 0. Thus, only a single-side, half channel-half landing setup had to be modelled to capture the GDL compression and electrical conduction effects, which is the scope of this study. A picture of the modelled domain is given in Fig. 13. The average cell compression pressure on the active area of the flowfield including landings and channels was set to 0.4 MPa, the same value as used in the cell experiments. For solving the model equations, COMSOL Multiphysics FEM-software was used because of its capability of coupling different physical modes like structural and electrical simulation. After the structural model was solved, the electrical properties of the GDL were locally matched using the measured dependencies. In-plane conductivity of the GDL fibre substrate was assumed to scale linearly with compressive strain ε_y, through-plane conductivity of the substrate and isotropic conductivity of the sublayer were expressed as a fitted function of local compression pressure based on the measurements presented in Section 4. Unlike in the mechanical part of the simulation, the GDL was subdivided into two domains with differing properties that are GDL fibre substrate and sublayer. The sublayer or microporous-layer was assumed to be electrically isotropic and 40 μm thick for all samples, which is consistent with measurements and manufacturer data sheets in an error span of approx. 5 μm. The sublayer conductivity was calculated based on the measurement presented in Section 4.3, also incorporating the contact resistance between catalyst layer and sublayer. Although a more distinct determination between both would be preferable, the effect on voltage loss was found to be equivalent based on simulation results. The contact resistance between GDL and flowfield plate has not been considered in the simulation. The electric potential at the GDL–flowfield boundary was set to 0 using a Dirichlet boundary condition.

For evaluation of the voltage loss through the GDL, a constant current density of 1 A cm^{-2} was assumed to enter the GDL at the catalyst layer interface using a Neumann boundary condition. Although this current density distribution is influenced by various effects like mass transport and local membrane humidity in reality, the assumption offers a good starting point to estimate electrical conduction effects separated from other factors of impact and allows quicker and simpler modelling. Effects of compression on mass and heat transport in the GDL have also been measured and will be presented as complete coupled model in the next study.

The simulated channel and landing geometries were taken from the flowfield dimensions of the cell used for the experimental cell results presented in Fig. 1. The channel width was set to 2.3 mm and the landing width was 0.7 mm. Both were included half in the modelling domain due to the stated symmetry constraints.

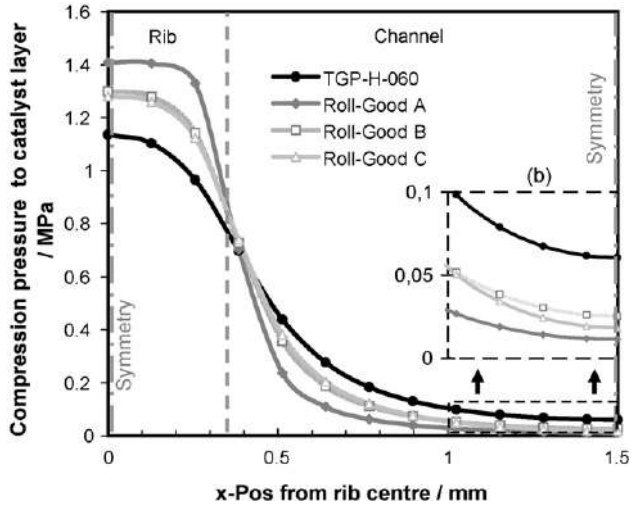

Fig. 14. (a) Simulated GDL compression pressure exerted to the catalyst layer. Plot starts at the catalyst beneath the flowfield rib centre (left) and continues to the channel centre (right). (b) Magnified plot of channel centre conditions.

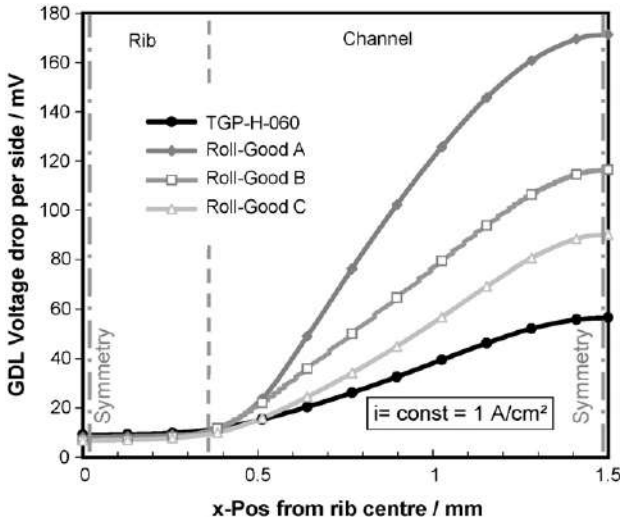

Fig. 15. Simulated local voltage drop over the GDL including catalyst contact per cell side at i = const = 1 A cm^{-2}. Plot starts at the catalyst beneath the flowfield rib centre (left) and continues to the channel centre (right).

For all simulated GDL samples, the stiffer fibre main direction was assumed to be orientated perpendicular to the channel direction.

5.2. Mechanical modelling results

The results of the mechanical modelling study showed a significant difference in the compression distribution between the batch produced TGP-H-060 and the roll-good GDL materials, as was expected from the considerations in Section 1. In Fig. 14a, the pressure exerted by the different GDL materials to the catalyst layer along the catalyst-sublayer boundary is depicted for the stated flowfield geometry. The plot starts at the centre of the flowfield rib and continues to the centre of the channel, wherein the rib edge would be found at an x-position of 0.35 mm. It is clearly found that using TGP, a more homogeneous pressure distribution is achieved compared to the roll-goods, with lower pressures under the rib and higher compression pressures under the channel. To highlight the conditions in the critical low compression zone around the channel centre, a zoom-in graph of the pressure distribution is shown in Fig. 14b. It is obvious that all materials reach a state of low compression below 0.1 MPa in the channel centre at 2.3 mm channels that can be regarded as critical in terms of electrical losses when compared to resistance curves given in Figs. 10 and 12. However, pressure exerted by the roll-goods is significantly lower in the channel centre compared to TGP-H-060. A parameter variation study showed that this is mainly due to the reduced shear modulus of those materials, which was found to be the parameter of highest impact on pressure homogeneity. However, the pressure exerted by roll-good GDL C is slightly lower in the channel centre compared to roll-good GDL B, in spite of the slightly higher shear modulus of the first. This can be accounted to its stiffer compression properties that cause steeper decrease of compression to the channel centre.

5.3. Coupled electrical modelling results

Coupling of structural simulation results to the electrical evaluation showed a drastic potential drop increase across the GDL and catalyst layer interface towards the channel centre for all GDL types. In Fig. 15, the local GDL potential drop per side of the MEA is depicted from the flowfield landing centre to the channel centre assuming a constant current density of 1 A cm^{-2}. The pressure and potential drop condition in the channel centre is compared explicitly in Fig. 16. The major dependency of voltage loss on material compression is obvious. However, in the case of roll-good GDL B and C, a slightly lower compression of type C does not lead to a higher voltage loss, but is overcompensated by higher substrate in-plane conductivity and lower sublayer and catalyst layer contact resistance. Thus, the voltage drop is reduced compared to GDL type B.

A voltage loss of more than 100 mV per side might look dramatic at a first glance, particularly considering that for a symmetric setup, this value will apply to anode and cathode side and has to be doubled for total loss estimation. However, for the effective losses seen in the cell polarisation the geometric average of local potential drop over the channel–landing span is important. Furthermore, part of the loss could be compensated if the current distribution is not homogeneous but is elevated in the lower resistance landing zones, which, however, is typically hindered by mass transfer. The simulated total average voltage drop for symmetric anode and cathode GDL was calculated and is given in Fig. 17, assuming a constant current density of 1 A cm^{-2}. The results show a total GDL voltage drop between 60 mV for TGP and 160 mV for roll-good GDL type A under the given assumptions and geometric constraints. Furthermore, the

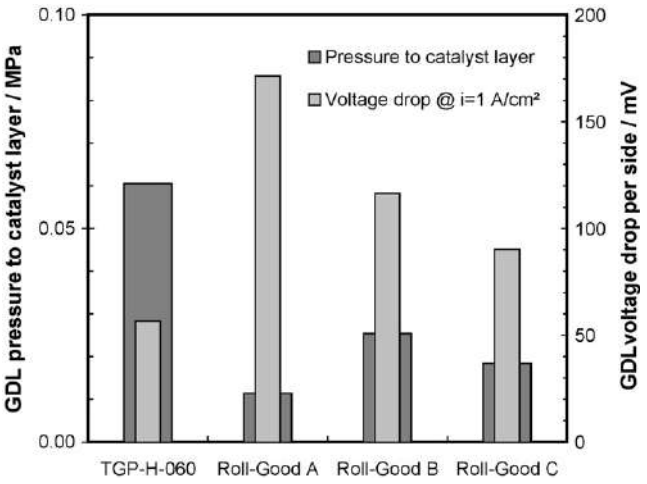

Fig. 16. Comparison of simulated local compression pressure and local voltage drop in the channel centre for different GDL materials.

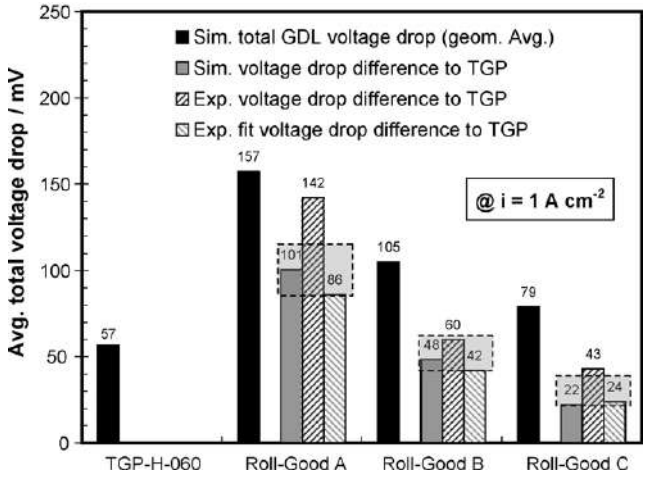

Fig. 17. Comparison of (1) simulated total geometric average voltage loss in the GDL for both cell sides at i = const = 1 A cm^{-2}. (2) Difference in simulated total voltage loss between TGP-H-060 and roll-good materials. (3) experimental voltage difference between TGP-H-060 and roll-good materials at 1 A cm^{-2}. (4) Voltage difference between TGP and roll-good materials for an extrapolated experimental fit curve between 0 and 500 mA cm^{-2} at 1 A cm^{-2} assuming constant Tafel slope and cell resistance.

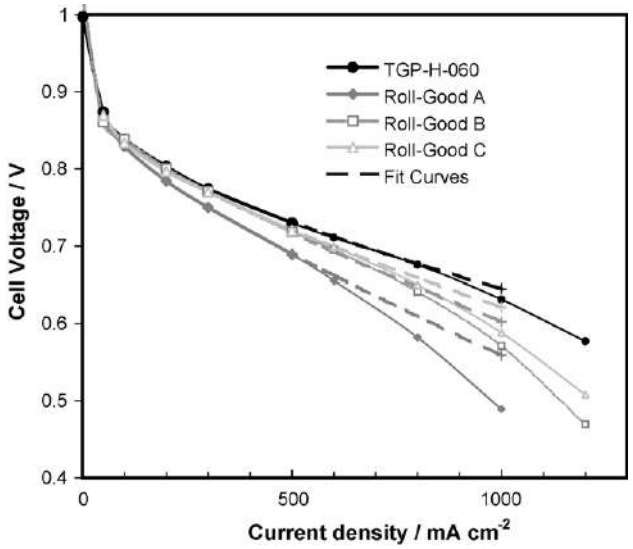

Fig. 18. Experimental polarisation curves for different GDL materials including extrapolated curve fit between 0 and 500 mA cm^{-2} (constant Tafel slope and resistance assumption).

simulated total voltage drop differences through the GDL between TGP and the roll-good materials are depicted and can be compared to experimental cell polarisation curves. The experimental cell voltage difference for the various materials, that can be taken from Fig. 1 is also shown. It is found that the mere mechanic-electrical simulation underpredicts the measured cell voltage difference at 1 A cm^{-2} significantly, in spite of the drastic voltage drop found in the channel centre.

5.4. Discussion

Taking a closer look at the experimental performance curves shows that especially the roll-good polarisations do not follow a nearly linear trend at 1 A cm^{-2} as it would be expected in the ohmic dominated region. Other effects must therefore be considered, as for example mass transport limitation or flooding that are typically stated in literature [3] as the reason for high-load progressive decline in polarisation voltage.

For this reason, a fitting approach based on the least square method was applied to the different experimental polarisation curves in the current range between 50 and 500 mA cm^{-2} assuming constant Tafel slope and constant cell resistance. It was assumed that the polarisation would be marginally influenced by the high load effects seen at 1 A cm^{-2} in that lower current region. The trend curves were extrapolated to the 1 A cm^{-2} point as shown in Fig. 18 to get unbiased polarisation values that can be compared. The difference between those extrapolated polarisation values for the different materials was also included in Fig. 17 and shows a very good agreement with the simulated performance differences. Thus, it can be assumed that mere ohmic effects are captured well by the simulation approach presented. However, additional losses are generated in the high load regime with the regarded materials that are not comprised yet.

These additional losses could possibly be attributed to mass transport limitations, which can become even more pronounced if the local current density is elevated under the landings due to high electrical resistance under channel sections for roll-good materials. Additional losses can be generated by local membrane overheating due to inferior GDL thermal conductivity or due to limited water management capabilities of the alternative materials. The modelling results for a combined simulation of charge, mass and heat transfer in relation to simulated compression are beyond the scope of this paper, however.

6. Conclusions

This article investigates the local gas diffusion layer compression distribution in the flowfield of a PEM fuel cell and the associated electrical losses in zones of low compression for different material classes. The intention is to explain performance differences found for different material classes in cell polarisation measurements. For modelling of the compression distribution between flowfield landings and channels, an orthotropic material model for the fibrous gas diffusion layer in macroscopic approach is introduced and measurement methods are presented to evaluate the relevant material parameters. Measurement results are depicted for several diffusion layer materials and significant mechanical differences are outlined between economic roll-good materials and a batch produced paper (TGP-H-060). The parameter of highest impact for a homogeneous compression distribution is identified as the shear modulus that differs by a factor of up to 4 between the roll-good and the sheet materials. This parameter together with the measured bending and compression moduli leads to simulated GDL compression pressures exerted to the catalyst layer between 0.015 MPa for a roll-good and 0.06 MPa for TGP in the channel centre assuming wide channels of 2.3 mm span.

The simulated intrinsic compression distribution in the GDL is coupled to its electrical properties in a second modelling step. Measurement methods for evaluating the anisotropic GDL electrical conductivities are presented and results are shown for the mentioned material types. Especially material through-plane resistance and sublayer combined with catalyst layer contact resistance are found to be highly compression dependent and increase progressively at low compression pressures for all materials. Coupling of these measurement results to the mechanic simulation yields potential drop values of up to 170 mV per side in the GDL for the least compressed type in the very channel centre assuming a constant current density of 1 A cm^{-2}. However, the geometric average GDL voltage loss for both sides is estimated between 50 and 160 mV at this channel geometry. Differences between the materi-

als are in very good agreement with polarisation voltage differences found in real cell measurements, if the ohmic dominated regime is regarded. However, at higher current densities additional loss effects arise in the cell polarisation, that have to be explained using a coupled compression, electrical, heat and mass transfer simulation, which will be left for the next study. Additional work will also be required for a more reliable measurement of sublayer and catalyst layer contact resistance that is highly influential for presented results. This method should also allow distinguishing both properties.

Acknowledgement

The authors would like to acknowledge the fruitful discussions and contributions to this work by the colleagues at Daimler AG, Department of MEA and Stack Technology. Prof. Dr. W. Tillmetz and Prof. Dr. H. Kabza are thanked for scientific supervision of this study.

References

[1] H. Tsuchiya, O. Kobayashi, Int. J. Hydrogen Energy 29 (2004) 985–990.
[2] E.J. Carlson, P. Kopf, J. Sinha, S. Sriramulu, Y. Yang, Cost analysis of PEM fuel cell systems for transportation, NREL Report—NREL/SR-560-39104, 2005.
[3] M. Mathias, J. Roth, J. Fleming, W. Lehnert, Handbk. Fuel Cells (2003) (Chapter 46).
[4] S. Escribano, J.-F. Blachot, J. Etheve, A. Morin, R. Mosdale, J. Power Sources 156 (2006) 8–13.
[5] M. Khandelwal, M.M. Mench, J. Power Sources 161 (2006) 1106–1115.
[6] Pressurex Micro Surface Pressure Mapping System Specification Sheet, Sensor Products Inc., Madison, 2007.
[7] P. Zhou, C.W. Wu, G.J. Ma, J. Power Sources 163 (2007) 874–881.
[8] J. Ge, A. Higier, H. Liu, J. Power Sources 159 (2006) 922–927.
[9] P. Zhou, C.W. Wu, G.J. Ma, J. Power Sources 159 (2006) 1115–1122.
[10] W.-K. Lee, C.-H. Ho, J.W. Van Zee, M. Murthy, J. Power Sources 84 (1999) 45–51.
[11] P. Zhou, C.W. Wu, J. Power Sources 170 (2007) 93–100.
[12] N. Fekrazad, T.L. Bergman, J. Heat Transfer 129 (2007) 1004–1013.
[13] H. Meng, C.-Y. Wang, J. Electrochem. Soc. 151 (2004) A358–A367.
[14] J.G. Pharoah, K. Karan, W. Sun, J. Power Sources 161 (2006) 214–224.
[15] W. Sun, B.A. Peppley, K. Karan, J. Power Sources 144 (2005) 42–53.
[16] T. Zhou, H. Liu, J. Power Sources 161 (2006) 444–453.
[17] I. Nitta, T. Hottinen, O. Himanen, M. Mikkola, J. Power Sources 171 (2007) 26–36.
[18] T. Hottinen, O. Himanen, S. Karvonen, I. Nitta, J. Power Sources 171 (2007) 113–121.
[19] I. Nitta, O. Himanen, M. Mikkola, Electrochem. Commun. 10 (1) (2008) 47–51.
[20] T. Hottinen, O. Himanen, Electrochem. Commun. 9 (5) (2007) 1047–1052.
[21] S.A. Freunberger, M. Reum, J. Evertz, A. Wokaun, F.N. Büchi, J. Electrochem. Soc. 153 (11) (2006) A2158–A2165.
[22] R. Stark, Festigkeitslehre, Springer, Wien, 2006, Chapter III.
[23] N. Kikuchi, Finite Element Methods in Mechanics, Cambridge University Press, Cambridge, 1986 (Chapter V).
[24] W.F. Riley, L. Zachary, Introduction to Mechanics of Materials, John Wiley & Sons, New York, 1989.
[25] D. Gross, W. Hauger, P. Wriggers, Technische Mechanik Band, vol. 4, Springer, Berlin, 2007.
[26] H. Schürmann, Konstruieren in Faser-Kunststoff-Verbunden, Springer, Berlin, 2005.
[27] J.N. Reddy, C.S. Krishnamoorthy, K.N. Seetharamu, Finite Element Analysis for Engineering Design, Lecture Notes in Engineering, vol. 37, Springer, Berlin, 1988 (Chapter I: J.N. Reddy, A Review of the Equations of Mechanics & Chapter XIV: J.N. Reddy: Mechanics of Composite Structures).
[28] H. Ding, W. Chen, L. Zang, Elasticity of Transversely Isotropic Materials, Solid Mechanics and its Applications, vol. 126, Springer, Dordrecht, The Netherlands, 2006.
[29] H. Altenbach, J. Altenbach, R. Rikards, Einführung in die Mechanik der Laminat- und Sandwichtragwerke, Deutscher Verlag für Grundstoffindustrie Stuttgart, 1996.
[30] A.M. Sastry, X. Cheng, C.W. Wang, J. Thermoplastic Comp. Mater. 11 (3) (1998) 288–296.
[31] DIN 53121, Prüfung von Papier, Karton und Pappe - Bestimmung der Biegesteifigkeit nach der Balkenmethode, Deutsches Institut für Normung, Berlin, 1987.
[32] ISO 5628 Paper and Board—Determination of Bending Stiffness by Static Methods, International Organization for Standardization, 1990.
[33] EN 310 Wood-based panels, Determination of modulus of elasticity in bending and of bending strength, European Committee for Standardization, Bruxels, 1993.
[34] EN 13706-2, Reinforced plastics composites – Specification for Pultruded Profiles – Part 2: Methods of Test and General Requirements, European Committee for Standardization, Bruxels, 2002.
[35] M.M. Balaban, W.T. Jackson, Exp. Mech. 11 (5) (1971).
[36] H. Yoshihara, A. Matsumoto, Wood Sci. Technol. 39 (2) (2005).
[37] ASTM D 3044-94, Standard Test Method for Shear Modulus of Wood-based Structural Panels, American Society for Testing and Materials, West Conshohocken, 1994.
[38] ISO 15310, Fibre-reinforced Plastic Composites—Determination of the In-plane Shear Modulus by the Plate Twist Method, International Organization for Standardization, 1999.
[39] H. Yoshihara, Y. Sawamura, Holzforschung 60 (2006) 543–548.
[40] K. Schneider, B. Lauke, W. Beckert, Appl. Comp. Mater. 8 (1) (2001).
[41] ISO 14130, Fibre-reinforced Plastic Composites—Determination of Apparent Interlaminar Shear Strength by Short-beam Method, International Organization for Standardization, 1997.
[42] A.O. Shcherbakova, S.B. Sapozhnikov, Mech. Comp. Mater. 37 (3) (2001).
[43] A. Heinzel, F. Mahlendorf, O. Niemzig, C. Kreuz, J. Power Sources 131 (1–2) (2004) 35–40.
[44] K. Cooper, Through-thickness Membrane Conductivity Measurement for HTM Program: Issues and Approach, DOE HTMWG Meeting 14 September 2006, DOE Award No. DE-FC36-06GO16028.
[45] Ye.P. Mamunya, H. Zois, L. Apekis, E.V. Lebedev, Powder Technol. 140 (2004) 49–55.
[46] Toray Carbon Paper Specification Sheet, Toray Industries Inc., Advanced Composites Department, Tokyo, 2001 (revised May 16th).